Research on convective cooling and thermal protection characteristics of integrated dual-sided deflector system

Manman Zhang *, Yi Jiang, Yueguang Deng

Posted Date: 26 April 2024

doi: 10.20944/preprints202404.1760.v1

Keywords: launch vehicle; diversion technology; gas jet; water spray cooling; numerical simulation of flow field

 doi:10.20944/preprints202404.1760.v1

Article

Research on Convective Cooling and Thermal Protection Characteristics of Integrated Dual-Sided Deflector System

Manman Zhang *, Yi Jiang and Yueguan Deng

Beijing Institute of Technology, School of Aerospace Engineering, Beijing 100081, China
* Correspondence: 1304369127@qq.com

Abstract: Based on the goals of "high reliability, high frequency, rapid launch, and low cost" for space launch site, and drawing inspiration from the design principles of SpaceX's Starship launch test facility, an integrated dual-sided deflector system for convective cooling and thermal protection is presented. The interaction process between the gas jet and liquid water jet and its effect on the flow field environment are thoroughly studied using numerical calculation methods. Furthermore, Regarding the phase-change heat transfer issue in a compressible gas-liquid two-phase flow and the varying distribution of different bubble shapes and sizes at the gas-liquid interface, a modified Lee model is derived. The rationality and accuracy of the phase-change mass-transfer coefficient values can be improved by adjusting the equivalent diameter and shape factor of the bubbles. The research results demonstrate that compared to the classical Lee model, the modified Lee model can achieve a higher numerical accuracy in predicting the heat and mass transfer processes in gas-liquid two-phase flows. Through comparative analysis with traditional dual-sided deflector and conventional cooling system, the integrated dual-sided deflector system for convective cooling and thermal protection exhibits significant performance advantages in gas flow regulation, flow field environment improvement and erosion protection in the near-ground region of the launch site. Particularly, regarding the thermal environment of the dual-sided deflector, it not only achieves effective flow deflection, but also mitigates the degree of erosion caused by the gas jet on the deflector. This conclusion can provide theoretical references for the thermal protection design of commercial launch vehicle system at space launch site.

Keywords: launch vehicle; diversion technology; gas jet; water spray cooling; numerical simulation of flow field

I. Introduction

Launch vehicles are generally launched by thermal launching. The intense impact and erosion effects generated by the gas jets expelled from the rocket engine can significantly jeopardize the safety of the launch equipment and deflection devices. If the gas jets fail to be smoothly expelled, it can severely impede the proper functioning of the rocket's body and launch platform, and even lead to launch failures [1–3]. Therefore, research aimed at reducing the adverse effects of impact and erosion caused by the gas jet is of paramount importance in improving the performance of launch vehicle systems, reducing launch costs, and shortening launch cycles.

To reduce the intense thermal and dynamic impact effects of the rocket engine exhaust plume, aerospace launch sites both domestically and internationally typically employ gas jet impingement with water spray to cool down the flow field. Kennedy Space Center in Florida utilized a "deflector channel + water spray" approach to mitigate the exhaust plume generated during hot launching, which effectively reduced the adverse effects on the launch equipment [4,5]. The Ariane 5/6 launch site of the European Space Agency employed a "deflector channel + automatic four-stage water spray" system to guide and cool the gas jet. The second-stage water spray test for the Long March 7 launch

 doi:10.20944/preprints202404.1760.v1

platform had been successfully conducted at the Wenchang Spacecraft Launch Site in Hainan. The water spray system automatically activated during rocket launch, providing thermal and dynamic impact protection for the launch platform. Li et al. conducted numerical simulations and related experiments using a multiphase flow mixing model to investigate water injection into rocket engine plumes [6]. Lu et al. compared the cooling effects of two different levels of water spray systems on the launch pad for the Long March 7 rocket, indicating that the cooling area of each nozzle decreased as it got closer to the central region [7]. Zhou et al. conducted numerical studies on the gas flow field of launch vehicle and analyzed the influence of different water spray angles on the cooling effect, which provided theoretical references for the design of cooling systems in launch sites [8–10]. Ji developed a scaled-down model of a launch vehicle, numerically simulated the gas-water spray flow field, and studied the effects of water spray intensity and droplet diameter on temperature improvement [11]. Xiong performed numerical simulations of water spray cooling on the test stand for ground ignition tests of rocket engines using computational fluid dynamics (CFD) methods. The feasibility and optimization of water spray cooling were investigated through theoretical research and numerical simulations [12]. Luo et al. conducted numerical simulations to study the noise reduction system and bottom cooling protection of the test stand, considering the mutual influence between the two aspects [13].

The conventional water spraying methods used in the launch sites effectively mitigate the pressure pulses, erosive effects caused by the rocket engine exhaust plume, and improve the temperature environment of the gas flow field. However, these methods have certain limitations. Firstly, the deflector and water spraying systems are separate and independent equipment, which results in complex structures, large facilities, numerous water pipelines, and low reusability. Secondly, the excavation, repair and modification costs of the deflector are high, making it unsuitable for high-density rocket launches, rapid response, and low-cost operations [14]. Additionally, the energy in the high-temperature core region of the gas plume does not propagate outward or does so to a limited extent, when water is sprayed from the side and directed downward onto the gas plume. The heat transfer efficiency within the gas phase flow field is much lower than the interphase heat transfer efficiency. As a result, the energy in the core region of the gas plume remains unchanged, and the improvement in the erosion and scouring of the deflection device by the gas plume is not significant.

Based on the analysis above and drawing inspiration from the design concept of using "water-cooled steel plates" at the SpaceX Starship launch test site, a thermal protection and cooling system called the "integrated dual-sided deflector system for convective cooling and thermal protection" is proposed. The study focuses on a specific model of a single-nozzle commercial launch rocket and its dual-sided deflector [15]. Computational fluid dynamics (CFD) numerical simulation methods are employed to investigate the fundamental mechanisms of the integrated dual-sided deflector system in improving the thermal launch flow field environment of the launch vehicle. The analysis primarily examines changes in flow field characteristics and the level of load impact on the deflector caused by the gas jets. A comparative analysis is conducted between the integrated dual-sided deflector system, traditional dual-sided deflector (without any heat protection and cooling measures), and conventional heat protection and cooling system (using water spraying from the side and directed downward). The purpose is to validate the feasibility of the integrated dual-sided deflector system in actively protecting the deflector from thermal effects and demonstrate its effectiveness in heat protection.

II. The Basic Physical Model

Gas jet flow and water spray cooling are typical turbulent flow problems in aerospace engineering, which involves various physical and mathematical models, such as the basic control equations, species transport equations, turbulence equations, multiphase flow models, and vaporization models. Mature CFD technique is used for numerical simulations of the gas flow field [16]. The control equations of the flow field are solved using the finite volume method, employing a second-order upwind scheme in spatial discretization and a first-order backward difference scheme

 doi:10.20944/preprints202404.1760.v1

in time discretization. The resulting system of algebraic equations is solved using prediction and multi-step correction methods. Due to space limitations, the focus will be on providing a detailed description of the vaporization model for liquid water.

The interaction between gas jet and liquid water, leading to vaporization phenomena, is a typical compressible gas-liquid multiphase flow problem. It has been demonstrated in Ref. 6 and Ref. 16 that the Euler-Euler approach with the Mixture two-phase flow model can accurately simulate the mixing process of gas and liquid phases. Therefore, the Mixture model is chosen to investigate compressible two-phase flow phenomena involved in gas jet flow and water spray cooling. The vaporization and condensation phenomena of liquid water are incorporated into the mass equation of water vapor as a mass source term, resulting in the following expression:

$$\frac{\partial}{\partial t}\left(\alpha_v \rho_v\right)+\nabla\cdot\left(\alpha_v \rho_v \mathbf{v}_v\right)=\dot{m}_{lv}-\dot{m}_{vl}\,, \quad (1)$$

where the subscript v is water vapor, α_v is the volume fraction of water vapor within the control volume, ρ_v is the density of water vapor, v_v is the velocity of water vapor in the gas phase, m_{lv} is the vaporization rate, and m_{vl} is the condensation rate.

Based on the research by Lee, the mass transport rate (vaporization and condensation) of water can be related to temperature as follows [17]:

$$\begin{cases}\begin{cases}\dot{m}_{lv}=\text{coeff}\cdot\alpha_l\rho_l\dfrac{\left(T_l-T_{sat}\right)}{T_{sat}}, & T_l\geq T_{sat}\\ \dot{m}_{vl}=0\end{cases}\\ \begin{cases}\dot{m}_{lv}=0\\ \dot{m}_{vl}=\text{coeff}\cdot\alpha_v\rho_v\dfrac{\left(T_{sat}-T_v\right)}{T_{sat}}, & T_v<T_{sat}\end{cases}\end{cases}, \quad (2)$$

where coeff is the phase change mass transfer coefficient, T_l is the temperature of liquid water, T_{sat} is the saturation temperature corresponding to the current pressure, T_v is the temperature of water vapor, and α_l, α_v, ρ_l and ρ_v are the volume fractions and densities of the liquid and vapor phases within the computational cell, respectively.

By combining the Hertz-Knudsen formula and the Clausius-Clapeyron equation, the expression for the phase change mass transfer coefficient in Eq. 2 can be obtained as follows [18-21]:

$$\text{coeff}=\frac{6}{d_b}\beta\sqrt{\frac{M}{2\pi RT_{sat}}}L\left(\frac{\alpha_v\rho_v}{\rho_l-\rho_v}\right), \quad (3)$$

where d_b is the bubble diameter of water vapor, and β is the sticking coefficient which represents the fraction of water vapor absorbed by water.

Indeed, the phase change mass transfer coefficient is typically assumed to be an empirical constant, when using the classical Lee phase change mass transfer equation. However, there is significant variation in the values reported in different literature sources [22–24]. The range of values is also quite wide, ranging from 0.1 to 10^7 s^{-1}. Furthermore, these values are based on empirical observations and have not been thoroughly analyzed for rationality or underlying physical mechanisms. In addressing the issue of relying on empirical values for the phase change mass transfer coefficient, Qiu et al. extensively considered factors such as fluid density, heat flux density, and specific enthalpy, which developed a steady-state analysis model to examine the influence of different mass transfer coefficient values on the simulation results of phase change heat transfer [25]. Through analyzing the patterns of these influences, they derived reasonable values for the mass transfer coefficient. Guang et al. derived an explicit expression for calculating the phase change mass transfer coefficient in the Lee model [26]. This expression clearly revealed the dependence of the mass transfer coefficient on various fluid properties (such as the density of the gas-liquid phases, thermal conductivity, latent heat, saturation temperature, etc.) and grid size. It also indicated that within a specific computational cell of the fluid, the value of the mass transfer coefficient depended on the volume fraction of the liquid phase. Furthermore, the maximum value of this coefficient corresponded to the minimum volume fraction of the liquid

 doi:10.20944/preprints202404.1760.v1

phase. Wang et al. took the classical Lee model mass transfer equation as a starting point and derived a new mass transfer coefficient model [27,28]. This model primarily considered the influence of normal and tangential concentration gradients at the gas-liquid interface on the mass transfer rate, which could be used to predict the mass transfer coefficient on the liquid side under turbulent conditions. The mentioned studies have addressed the issue of relying on empirical values for the phase change mass transfer coefficient and lack of theoretical basis in existing literature. However, few studies have considered the bubble parameter factor in deriving and modifying the calculation formulas for the mass transfer coefficient. This neglect the influence of varying distributions of different bubble shapes and sizes at the gas-liquid interface on the heat and mass transfer processes. The bubble parameter factor is an important piece of information that reveals the mass and heat transfer mechanisms between the gas and liquid phases. Existing mass transfer correction models have limited ability to accurately describe the relationship between the bubble parameters and the phase change mass transfer coefficient, and its application scope remains limited.

In the analysis of boiling and evaporation scenarios, bubbles are generated, which carry away some heat during the liquid-phase endothermic evaporation process. These bubbles vary in size and shape, which have an impact on the phase change mass transfer coefficient [29–31]. Additionally, the saturation temperature of the fluid will vary under different pressure conditions, thereby affecting the heat exchange process during the evaporation phase change in the gas-liquid two-phase flow. Therefore, it is necessary to consider the bubble parameter factor and make modifications and improvements to Eq. 2 and Eq. 3, which is to enhance the accuracy of the phase change mass transfer coefficient in numerical simulations of gas-liquid two-phase flow fields.

In turbulent flow conditions, the liquid water surface experiences forces from different directions when in contact with high-temperature and high-velocity gas jets. Consequently, the vapor bubbles generated during liquid evaporation are not perfectly spherical but can also exhibit non-spherical shapes, such as ellipsoidal shapes. Assuming the ellipsoid has three semi-axes a, b, and c, the volume of the ellipsoid is $V = 4/3\pi abc$, and the surface area is $S = 4/3\pi(ab+bc+ac)$. In this case, the d_b in Eq. 3 can be replaced by the following expression:

$$\frac{4/3\pi\left(ab+bc+ac\right)}{4/3\pi abc}=\frac{1}{a}+\frac{1}{b}+\frac{1}{c}, \quad (4)$$

and the expression for the mass transfer coefficient corresponding to an ellipsoidal bubble is given by:

$$\text{coeff}=\left(\frac{1}{a}+\frac{1}{b}+\frac{1}{c}\right)\beta\sqrt{\frac{M}{2\pi RT_{sat}}}L\left(\frac{\alpha_v\rho_v}{\rho_l-\rho_v}\right). \quad (5)$$

When both spherical and ellipsoidal vapor bubbles exist, their proportions are related by a certain ratio. Assuming the proportion of spherical bubbles is denoted as e, the expression for calculating the phase change mass transfer coefficient is as follows:

$$\text{coeff}=\left[e\frac{6}{d_b}+(1-e)\left(\frac{1}{a}+\frac{1}{b}+\frac{1}{c}\right)\right]\beta\sqrt{\frac{M}{2\pi RT_{sat}}}L\left(\frac{\alpha_v\rho_v}{\rho_l-\rho_v}\right). \quad (6)$$

To further simplify Eq. 6, the expression can be described as follows:

$$\text{coeff}=\frac{\theta}{d_e}\beta\sqrt{\frac{M}{2\pi RT_{sat}}}L\left(\frac{\alpha_v\rho_v}{\rho_l-\rho_v}\right), \quad (7)$$

where d_e is the equivalent diameter of the spherical or ellipsoidal bubble, and θ is the shape factor which is dependent on temperature and pressure [29–31].

Furthermore, considering the influence of the pressure at the gas-liquid interface on the saturation temperature T_{sat}, the modified and improved Lee theory model can be expressed as follows:

 doi:10.20944/preprints202404.1760.v1

$$\begin{cases} \dot{m}_{lv} = \text{coeff} \cdot \alpha_l \rho_l \dfrac{\left(T_l - T_{sat}(P)\right)}{T_{sat}(P)} \\ T_l \geq T_{sat}(P) \\ \dot{m}_{vl} = \text{coeff} \cdot \alpha_v \rho_v \dfrac{\left(T_{sat} - T_v(P)\right)}{T_{sat}(P)} \\ T_v < T_{sat}(P) \end{cases}, \quad (8)$$

$$\text{coeff} = \frac{\theta(T,P)}{d_e} \beta \sqrt{\frac{M}{2\pi R T_{sat}}} L \left(\frac{\alpha_v \rho_v}{\rho_l - \rho_v} \right), \quad (9)$$

$$e = \frac{\theta(T,P) \cdot \lambda - \lambda^3 \cdot d_e^{\,3}}{6 - \lambda^3 \cdot d_e^{\,3}}, \quad (10)$$

where T、P are the temperature and pressure of the gas-liquid interface grid cell, λ is a dimensionless coefficient related to the diameter [32–34]. Based on the classical Lee model, a gas-liquid phase change mass transfer model that considers bubble parameter factors can be derived. By adjusting the equivalent diameter of the bubble d_e and the shape factor θ, the rationality and accuracy of the phase change mass transfer coefficient can be achieved.

By compiling Eq. 8, Eq. 9 and Eq. 10 in the C programming language and using Fluent's User Defined Functions (UDFs), it is possible to implement the modified Lee model within the Mixture multiphase flow model. By incorporating the improved Lee model and leveraging relevant experimental data, it is possible to determine the range of values or empirical formulas for the phase change mass transfer coefficient, considering the bubble parameter factors. This approach allows for an enhancement in the accuracy of numerical simulations for gas-liquid multiphase flows.

III. Numerical Simulation Models

A. Physical Model Design

Based on the objectives of "low cost, high reliability, high frequency, and rapid launch", this study focuses on a small-scale commercial launch vehicle with a single nozzle and its double-sided deflector [15]. The original geometric model of the launch vehicle is too large and structurally complex, resulting in a large physical model and computational domain. It not only increases the number of grid cells but also extends the computational time and data storage space. To address these challenges without affecting the initial gas diffusion flow and smooth exhaust during the launch phase, the structural dimensions of the original geometric model of the rocket and launch site are appropriately reduced and simplified, as shown in Figure 1. Additionally, a cartesian coordinate system is established, with the origin *o* located at the center of the bottom cross-section of the rocket. The *oy*-axis is oriented vertically upward, the positive direction of the *ox*-axis is as shown in Figure 1, and the *oz*-axis is determined by the right-hand rule. Based on the simplified boundaries of the physical model, the computational domain for the flow field is established. Due to the geometric symmetry of the launch vehicle and deflector, the 1/2 model is used for numerical simulations of the flow field. The dimensions of the computational domain are 65*De* × 13*De* × 12*De*, where *De* is the nozzle exit diameter. During the rocket launch process, the vertical direction (*y*-direction) is only considered for single-degree-of-freedom motion.

 doi:10.20944/preprints202404.1760.v1

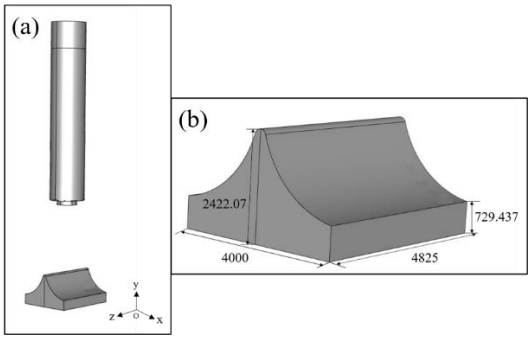

Figure 1. Geometric model of the launch vehicle and its double-sided deflector: (a) overall model; (b) locality model- deflector.

Currently, both domestic and international aerospace launch sites have developed mature conventional cooling systems, in which water spray devices are generally located above the deflector trough on the launch platform or in lateral positions around the launch platform. The water spray system is typically designed with a combination of multiple stages, high flow rates, and automatic control. During rocket launches, water is sprayed from above downwards onto the gas jet for cooling purposes. The flow field model of the conventional heat protection and cooling system is shown in Figure 2, based on the model depicted in Figure 1. Considering practical engineering experience, a total of 48 water spray pipes are installed at a certain height circumferentially above the deflector. There are 14 pipes distributed along the long side (y-direction) and 10 pipes distributed along the short side (x-direction). The cross-sectional dimensions of the water spray pipes are 100mm × 100mm, with a length of 240mm. The angle between the pipes and the horizontal plane (parallel to the oxz plane) is 60°.

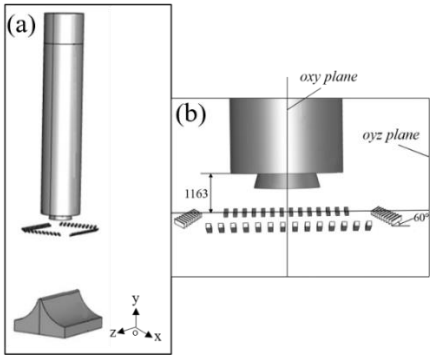

Figure 2. The model of the conventional cooling system: (a) overall model; (b) the bottom of the rocket.

Based on the previous literature review, numerical simulations of gas flow fields and analysis of their variations, a new type of heat protection and cooling system called the integrated dual-sided deflector system for convective cooling and thermal protection is proposed to improve the thermal environment of rocket exhaust flow. The aim is to reduce the impact erosion intensity on the deflector caused by the gas jet and lower the temperature of the flow field. Building upon the traditional dual-sided deflector, a water spray system is integrated, as shown in Figure 3. This involves designing perforations on the deflector surface and adding liquid water nozzles, resulting in an integrated design of the deflector and water spray system. To ensure that the conventional cooling system and the integrated dual-sided deflector system have the same water discharge rate for the same operating time and the same liquid water velocity, a total of 135 liquid water orifices are distributed on the deflector surface. Specifically, one row of liquid water orifices is placed at the top of the dual-sided deflector, and four rows are evenly spaced from top to bottom on each side of the deflector, with 15

 doi:10.20944/preprints202404.1760.v1

orifices per row. The cross-sectional dimensions of the liquid water orifices are 60mm × 60mm. Depending on different working conditions, different liquid water orifices can be opened or closed. They can be set as wall boundary conditions when not needed, and be set as velocity inlet boundary conditions when required. Through the water spray system on the deflector, liquid water can be sprayed on the gas jet flow area in advance before the engine ignition to realize the effect of improving the flow field of the rocket thermal launch.

The working principle of the integrated dual-sided deflector system is shown in Figure 3(b). Multiple liquid water flow channels are laid inside the dual-sided deflector, with the ends of the channels connected to the orifices on the deflector surface and the water tank. During the initial phase of rocket launch and the thermal emission process, the liquid water injection pressure in the water tank is regulated [34,35]. On one hand, this ensures that the liquid water flows continuously from the orifices on the deflector surface into the space at the bottom of the rocket at a certain velocity. It provides sufficient liquid water to absorb and carry away the heat from the gas jets, creating a counter-flowing water jet. On the other hand, it ensures that the liquid water jet has enough kinetic energy to overcome the stagnation pressure (6-8 atm) caused by the impact of the gas jet on the deflector surface. This helps maintain the continuity and stability of the liquid water jet and ensures an effective convective impact between the counter-flowing liquid water jet and the gas jets. Moreover, the flow velocity and kinetic energy of the liquid water jet from the deflector surface can be controlled by adjusting the injection pressure of the liquid water. This increases the momentum transfer ratio and contact area between the gas-liquid two-phase flow, enhancing the convective impact and mixing cooling effect. It reduces the differences in local temperature and velocity, effectively improving the uniformity and stability of the gas flow field.

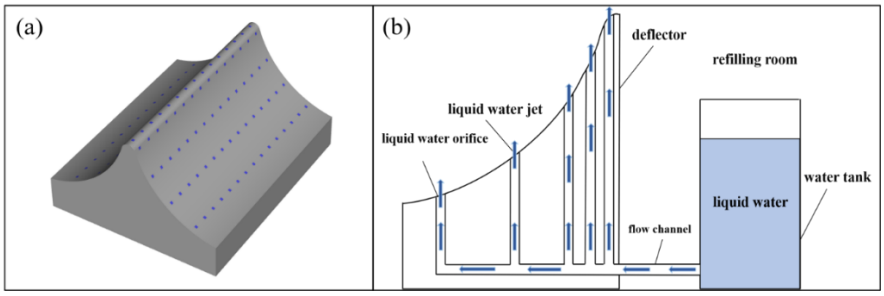

Figure 3. The integrated dual-sided deflector system for convective cooling and thermal protection: (a) overall model; (b) working principle.

B. Grid Generation and Boundary Conditions

Considering the geometric complexity of the rocket structure, including the regularity of its shape and the curved surface of the dual-sided deflector, a structured/unstructured hybrid grid is adopted to partition the flow field region of the rocket exhaust. The grid size is determined based on specific structural features and overall scale, such as the liquid water orifices, throat of the nozzle, and the computational domain. Figure 4 illustrates the schematic of the flow field grid partition. A dynamic grid-layering method is employed to update the grid in the flow field region. The newly generated grids are located at the intermediate position between the bottom of the rocket body and the dual-sided deflector, as well as at the top surface of the rocket body. The grid size in the former region is smaller, while the grid size in the latter region is larger. To better capture the flow phenomena, including gas jet spreading, gas exhaust through the deflector, and the convective impact between the liquid water and high-temperature gas, the grids in the region of the bottom space of the rocket body, the surface of the dual-sided deflector, and the nearby ground are refined, as shown in Figure 4(b) and (c).

 doi:10.20944/preprints202404.1760.v1

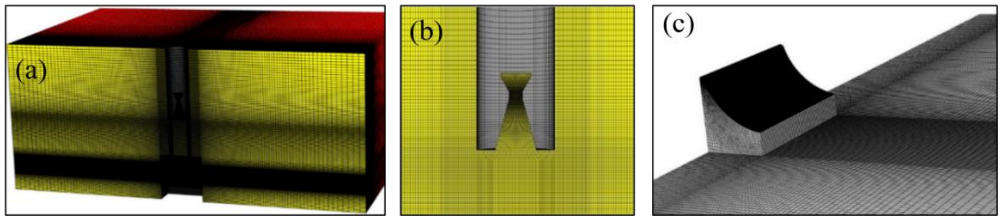

Figure 4. Grid modeling of the launch flow field: (a) overall grid; nozzle; (c) deflector.

The boundary condition settings for the flow field computational domain are as follows. The combustion chamber end face of the engine nozzle is set as the pressure inlet. The gas enters the flow field through this boundary, with a total gas temperature of 3638.83K. The pressure distribution in the high-pressure chamber is represented by the pressure ratio P/P_0, which is a dimensionless quantity. P_0 is the ambient pressure. The pressure profile is shown in Figure 5. The upper and side boundaries of the computational domain are set as pressure outlets. The ambient pressure is set to 101325Pa, and the ambient temperature is set to 300K. The surfaces of the engine, rocket body, ground, and dual-sided deflector are all set as no-slip adiabatic walls. When using the 1/2 model, there exists a set of symmetric boundary planes, as indicated by the yellow region in Figure 4(a). The liquid water orifices are set as velocity inlets. The liquid water is injected into the computational domain through these orifices with a velocity of 40m/s, a temperature of 300K, and a pressure of 101325Pa.

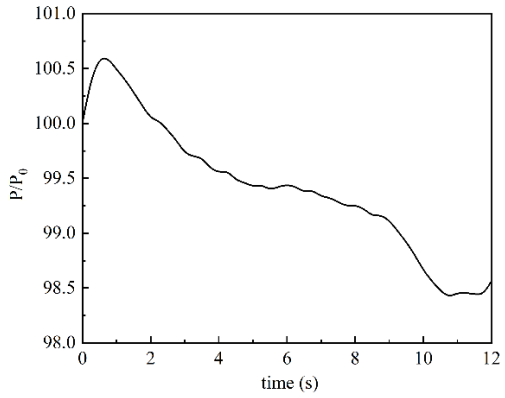

Figure 5. Pressure-time curve of the high-pressure chamber.

The thermal environment characteristics of the dual-sided deflector are a key focus in the numerical simulation of the flow field. Therefore, multiple monitoring points are established on the deflector surface to measure the temperature and dynamic pressure variations at these points. This allows for the evaluation of the deflector's resistance to erosive effects caused by the impingement of the gas jet. Figure 6 provides a schematic distribution of the monitoring points on the deflector surface. P11 to P41 are located at the top surface of the deflector. Among them, P11 is positioned on the axis of the rocket engine, while P21, P31, and P41 are equally spaced and located on one side of the top surface. P11, P12, P13, and P14 are located at the intersection between the symmetry plane and the deflector surface. P22, P32, P33, and P44 are respectively located at the midsection and downstream region of the deflector surface.

 doi:10.20944/preprints202404.1760.v1

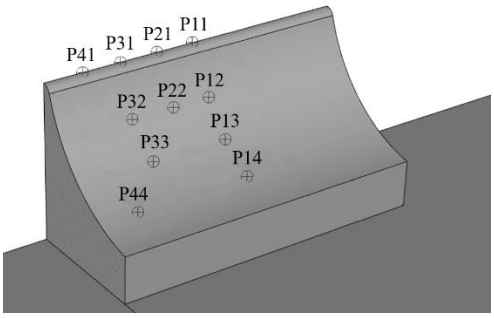

Figure 6. The monitoring points on the deflector surface.

C. Grid Independence Verification

When solving flow fields using the finite volume method, it is necessary to divide the computational domain into discrete grid cells. The size of the grid cells directly affects the accuracy of the numerical results during the discretization of the flow field. Selecting an appropriate grid size not only saves a significant amount of computational time, but also reduces computational resource costs. Therefore, conducting grid independence analysis is crucial when determining the grid size [16].

In Figure 3(a), the dimensions of the liquid water orifices on the deflector surface are 60mm × 60mm. These orifices represent the "smallest" structural features in the entire physical model. To accurately simulate the interaction between liquid water and the gas jet as well as the degree of water vaporization, a fine grid resolution is required. However, excessively fine grid divisions would result in a significantly larger number of grid cells within the entire computational domain, surpassing the current computational capacity. Furthermore, the dimensions of the nozzle throat, a critical location in the numerical simulation of gas jet formation and diffusion, have a significant impact on the accuracy of the gas jet numerical calculations. Based on the diameter of the nozzle throat and the grid size at the liquid water orifice location, four sets of grids were created with 4.44 million, 6.42 million, 8.74 million, and 10.92 million grid cells. The grid sizes at each location are shown in Table 1.

Table 1. Basic parameters of different grid numbers.

Parameters (mm)	The number of grid cells (million)			
	4.44	6.42	8.74	10.92
The dimensions of the nozzle throat	25	20	15	10
The dimensions of the liquid water orifices	12	10	8	6

Based on the previous multiple rounds of trial calculations and considering the vertical distance *L* between the top of the deflector and the exit section of the engine nozzle, as well as ensuring the effective functioning of the water spray system, the engine ignition is initiated after 40 ms of the water spray system operation. At this time, the reverse liquid water jet injected from the top position of the deflector has moved vertically to a height of 1/3 *L*. The ignition time of the engine is considered as t=0s for convenient comparison and analysis of the physical parameters in the flow field. The temperature data of monitoring points P32 and P33 on the deflector surface are extracted and compared for the time range of 0 to 0.5s, as shown in Figure 7. From the graph, it can be observed that the temperature curve of the 4.44 million grid model differs significantly from the other three curves. The temperature values of the monitoring points in the 6.42 million, 8.74 million, and 10.92 million grid models are relatively close, and the temperature curves of the 8.74 million grid model overlapping are more closely with the 10.92 million grid model. This indicates that after reaching a grid count of 8.74 million, further increasing the grid count has minimal impact on the numerical

 doi:10.20944/preprints202404.1760.v1

calculation results. Therefore, to improve computational efficiency while following the strategy of generating the minimum grid size, the division scheme with 8.74 million grid cells is adopted.

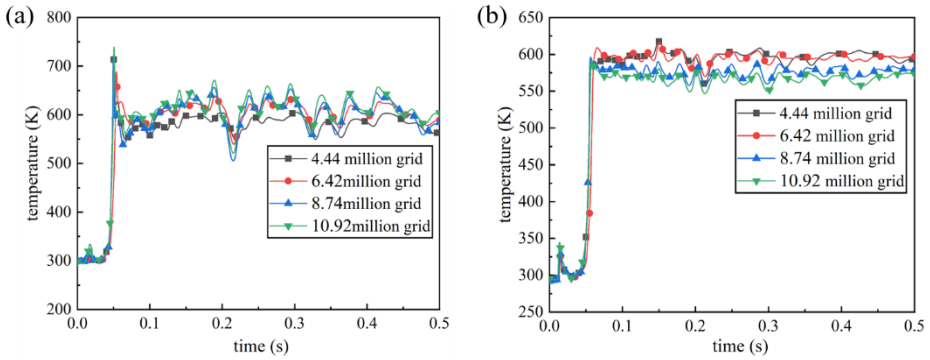

Figure 7. Temperature change curves of the deflector surface monitoring points: (a) monitoring point P32; (b) monitoring point P33.

D. Experimental Validation of the Vaporization Model

To validate the effectiveness and accuracy of the improved Lee model, numerical simulations are performed on the engine gas jet-water spray experiments conducted by Li et al. in an open environment [7,16]. The numerical simulations employ both the classical Lee model and the improved Lee model for vaporization modeling. In the experiment, four water spray nozzles were installed near the engine nozzle exit. The water spray nozzles were activated before the engine ignition, resulting in the convergence of four liquid water jets. After the engine ignition, the high-temperature gas jet impinged into the low-temperature liquid water, causing vaporization and heat absorption by the liquid water, thereby reducing the temperature of the flow field. Temperature sensors were placed at four locations (designated as A, B, C, and D) on the base plate. The temperature data at these four monitoring points were obtained using thermocouple sensors.

When there is no liquid water present in the gas flow field, that is, under no water spray conditions, a comparison between the wave structure of the gas jet captured by high-speed photography and the numerical simulation results is shown in Figure 8. In the figure, y is the axial distance from the nozzle throat to the wave node, and y_{max} is the maximum axial distance of the fourth wave node from the nozzle throat. From the graph, it can be observed that the positions of the first three clear wave nodes in the numerical calculation match well with those captured in the experiment which indicates that the numerical calculation method employed for the gas jet is reliable and accurate.

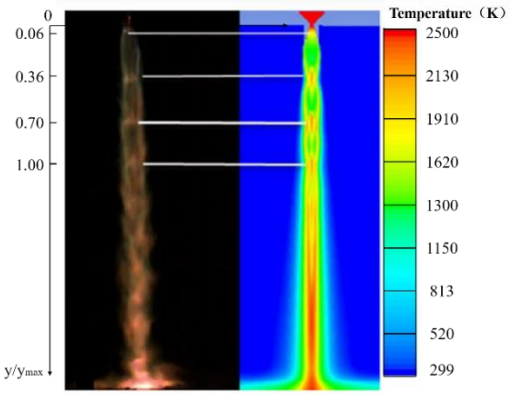

Figure 8. Comparison of wave structure comparison between the test shooting (left) and the numerical simulation (right).

 doi:10.20944/preprints202404.1760.v1

When the gas jet impacts the liquid water jet, intense vaporization of the liquid water occurs, resulting in a large amount of water vapor. The gas, air, and water vapor components continuously mix in the flow field. During the mixing process of the gas-liquid two-phase flow, there are also phenomena such as the movement, deformation, and breakup of the two-phase interface, which consume a significant amount of energy in the flow field. To accurately simulate the interaction between the gas jet and liquid phases in the gas-liquid two-phase flow, the improved Lee model is compiled into a User-Defined Function (UDF) file using the C language and loaded into Fluent. The temperature and pressure data from the four monitoring points on the base plate are extracted accordingly. A thorough analysis is conducted to investigate the coupling relationship between the shape factor θ and the temperature and pressure at the monitoring points. This analysis aims to explore the extent to which the bubble parameter factor affects the cooling effect in the flow field. Assuming an equivalent bubble diameter d_e (with typical bubble diameters ranging from 10 to 50 μm) and taking β as 0.001, numerical simulations are performed to simulate the vaporization process of liquid water under different shape factor values.

Based on the comparative analysis between the numerical simulation results and experimental data, it is found that when the shape factor θ is within the range of 18 to 60, it can adapt to a wide range of temperature and pressure variations and has a good corrective effect. Therefore, the shape factor θ is set to 32 for the numerical study. The numerical simulation results using the improved Lee model are compared with the simulation results using the classical Lee model and the experimental data, as shown in Figure 9 and Table 2. Compared to the classical Lee model, the temperature results obtained from the numerical simulation using the improved Lee model show a higher level of agreement with the experimental data. The relative errors are all below 0.5%, indicating that the improved Lee model can significantly enhance the accuracy of numerical calculations for the heat and mass transfer processes in the gas-liquid two-phase flow.

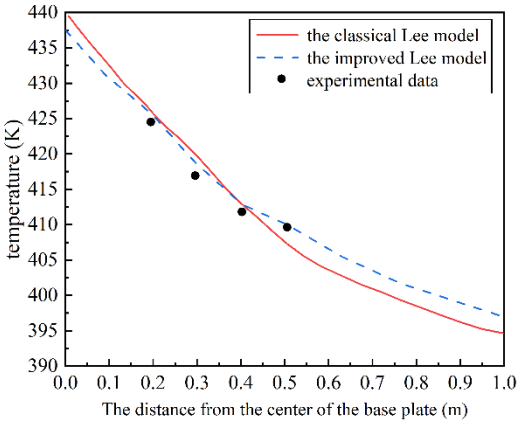

Figure 9. Comparison of the experimental measurement values and the numerical simulation values.

Table 2. Relative errors of temperature values at monitoring points between experimental data and simulation values.

monitoring points	experimental data	the classical Lee model	the improved Lee model
A	-	0.292%	0.291%
B	-	0.743%	0.443%
C	-	0.339%	0.271%
D	-	0.567%	0.101%

 doi:10.20944/preprints202404.1760.v1

IV. Numerical Computation and Result Analysis

A. Effectiveness of Gas Flow Control

The characteristics of gas flow directly impact the aerodynamic behavior of the rocket's surrounding flow field, including key factors such as drag, stability, control performance of the rocket's motion, and the safety of the launch system. This section focuses on investigating the influence of an integrated dual-sided deflector system on the gas diffusion flow and exhaust guidance effectiveness during rocket launch. Through comparative analysis with conventional cooling systems, the feasibility and superiority of the integrated dual-sided deflector system in regulating gas flow processes are validated.

Figure 10 illustrates the gas flow process within the *oxy*-symmetric plane influenced by the integrated dual-sided deflector system. The black contour lines represent the volume fraction of liquid water, indicating the presence of liquid water in the flow field and the mixing process between liquid water and the gas jet. At the initial moment of engine ignition, the high-temperature gas and the liquid water jet move towards each other. When the vertically downward gas jet interacts with the vertically upward "fountain" flow of the liquid water jet, the liquid water consumes and cools the gas in the "first round" of energy expenditure. Simultaneously, the liquid water changes its initial flow direction under the strong impact of the gas jet. As the gas diffusion flows towards the deflection surface region, the liquid water exhibits a "W-shaped" distribution along the deflector surface. Subsequently, the gas and liquid water rapidly diffuse to the ground position, forming the first wave node of the gas jet. The top of the deflector is in the high-temperature core region of the gas jet. At this point, the liquid water exhibits an "hourglass" distribution along the deflector surface and spreads over the surface of the deflector. As the launch vehicle accelerates to higher altitudes, the second and third wave nodes of the gas jet form successively, and the main flow of the gas jet fully develops. The core region of the gas jet begins to detach from the deflector. Meanwhile, the liquid water has spread over the deflector surface and the nearby ground area, forming a thick "water film" and providing a "second round" of insulating and cooling effect. The impact of the gas jet on the ground launch system and launch environment is significantly reduced. In the near-ground flow field influenced by the integrated dual-sided deflector system, due to the convective impact between the gas and liquid water jets, the liquid water flows in forms such as "fountain", "W-shaped", and "hourglass". There is a clear boundary between the gas and liquid phases, and throughout the entire process from the initial contact of liquid water with the gas to the end of the numerical calculation, the liquid water remains attached beneath the main flow of the gas jet. This facilitates an increase in the contact area and mixing degree between the gas and liquid phases, while better utilizing the thermal insulation and cooling effect of the liquid water.

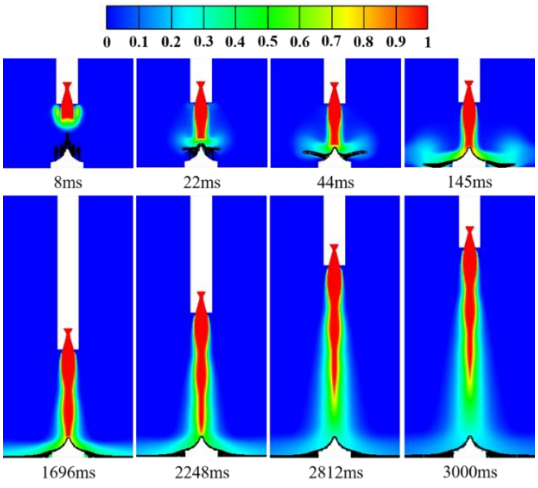

Figure 10. Gas flow process in the *oxy* symmetry plane under the integrated dual-sided deflector system, and the black contour in the figure is the volume fraction of liquid water with values ranging from 0 to 0.2.

 doi:10.20944/preprints202404.1760.v1

Figure 11 depicts a comparison of the gas distribution cloud maps between the conventional cooling system and the integrated dual-sided deflector system. From the figure, it can be observed that under both schemes, the rocket's motion process and trajectory are essentially the same, and the gas jet in the bottom space of the rocket is effectively guided and directed. In the conventional cooling system, the rate of gas diffusion into the surrounding space is somewhat reduced, leading to a prolonged duration of gas impinging on the deflector. However, the deflector and the nearby ground area still remain enveloped in high-temperature gas for an extended period. Therefore, the improvement in reducing the accumulation of high heat flux density in the near-ground flow field is not significant. On the other hand, the integrated dual-sided deflector system may exhibit relatively weaker performance in delaying the initial impingement of the gas jet on the deflector. However, through the gas jet and liquid water jet convective impact process and deflector surface formation of the "water film" (Figure 10), the integrated dual-sided deflector system can effectively disperse and diffuse the gas jet. This significantly reduces the contact area and contact time between the gas and the deflector, thus alleviating the accumulation of high-temperature gas in the near-ground flow field. As a result, the deflector is protected from the strong impact of the gas jet, achieving effective control over the gas flow process. In summary, the integrated dual-sided deflector system demonstrates advantages over the conventional cooling system in regulating the gas jets.

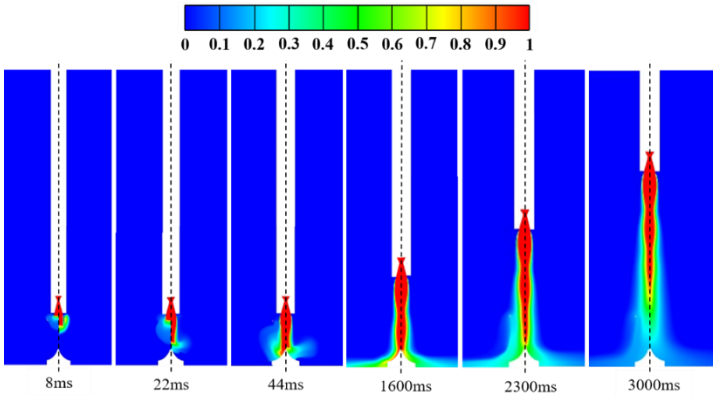

Figure 11. Comparison of gas flow process under the integrated dual-sided deflector and the conventional cooling system (the left side is the conventional cooling system, and the right side is the integrated dual-sided deflector).

B. Improvement in the Flow Field Environment

When the flow characteristics of the gas and its deflection effects are optimized and controlled, the near-ground flow field environment at the launch site undergoes changes, including the propagation of pressure disturbances, temperature variations, and the degree of liquid water vaporization. These changes directly impact the design of ground launch facilities and structures. This section focuses on studying the influence of the integrated dual-sided deflector system on the improvement of the gas flow field environment. By comparing and analyzing the temperature/pressure distribution characteristics of different thermal protection and cooling schemes, the superior performance of the integrated dual-sided deflector system in convective cooling, thermal protection, and improvement of the gas flow field environment can be demonstrated.

(1) Propagation of Pressure Disturbances

The pressure disturbances generated by the engine nozzle typically propagate through the fluid medium in the form of initial shockwaves and spread to the surrounding space. The propagation characteristics and process of these disturbances are greatly influenced by the properties of the medium and the surrounding environmental conditions. Figure 12 illustrates the pressure distribution within the flow field affected by the integrated dual-sided deflector system. From the figure, it can be observed that after the ignition of the engine, the initial shockwave interacts with the

 doi:10.20944/preprints202404.1760.v1

liquid water jet injected from the orifices located at the top of the deflector at an extremely high speed. The water jet is "captured" by the shockwave and vertically compressed downwards. Phenomena such as structural disruption of the water jet and localized vibration of water molecules consume a significant amount of energy from the shockwave [36]. When the first high-pressure wave node of the gas jet reaches the top region of the deflector, the initial shockwave has propagated to a distant ground location away from the deflector, resulting in a significant weakening of the shockwave intensity. The second high-pressure wave node of the gas jet then appears and forms. At this point, the liquid water covers the top and mid-body regions of the deflector, forming a "W-shaped" distribution along the contour of the deflector. As the rocket continues to accelerate to higher altitudes, the gas jet fully develops, and there is no longer the propagation of shockwaves within the flow field. The spatial distribution of pressure at the bottom of the rocket becomes relatively uniform, and the high-pressure region at the top of the deflector disappears. At this stage, the liquid water has completely covered the surface of the deflector and the surrounding ground area.

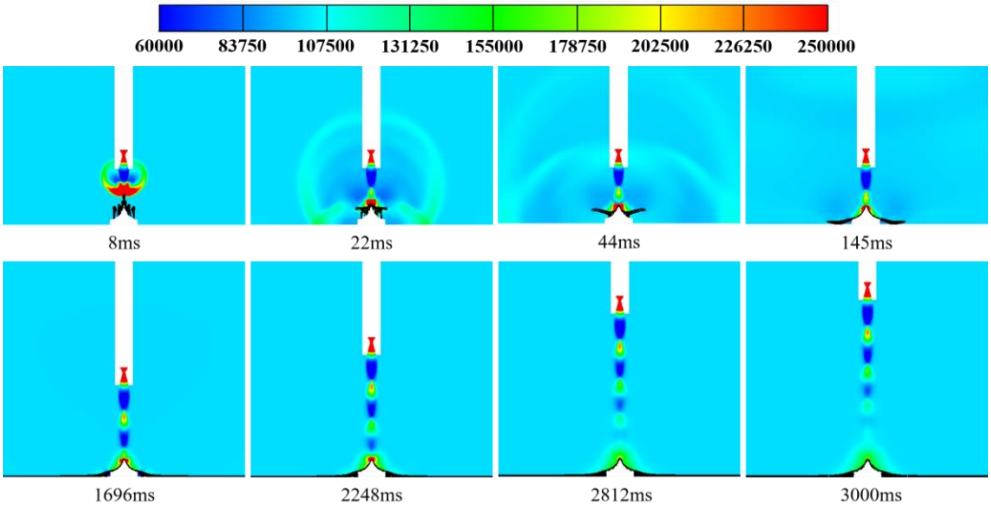

Figure 12. Pressure distribution in the *oxy* symmetry plane under the integrated dual-sided deflector system (unit: Pa), and the black contour in the figure is the volume fraction of liquid water with values ranging from 0 to 0.2.

Figure 13 illustrates a typical moment of comparison between the pressure distribution of the conventional cooling system and the integrated dual-sided deflector system. From the figure, it can be observed that the conventional cooling system has a suppressing effect on the initial shockwave. The energy propagation of the shockwave is reduced, especially during the initial ignition of the engine, where the speed and intensity of the shockwave propagation are significantly delayed. As a result, the near-ground pressure environment experiences some improvement. However, a considerable area of the deflector surface is still affected by the pressure disturbances, and it remains in a high-pressure state for a prolonged period during the rocket launch. In comparison to the conventional cooling system, the integrated dual-sided deflector system exhibits a relatively weaker inhibitory effect on the propagation rate and shockwave intensity of the initial shockwave. However, the liquid water jet injected from the orifices on the deflector's surface can cover the deflector and the surrounding ground area. This provides a certain level of pressure relief protection to the deflector, significantly reducing the affected area by the pressure disturbances, primarily concentrated at the top and mid-body regions of the deflector. Additionally, when the shockwave propagates to the surface of the deflector, it disrupts the structure of the liquid water jet, causing deformation and spreading of the water jet. During this process, some of the energy of the shockwave is consumed. Furthermore, the inertia of liquid water is greater than that of gas, and the shockwave's energy is also partially consumed when it induces vibrations in the liquid water molecules through localized oscillations. The combined effect of these two mechanisms effectively weakens the dynamic load impact intensity of the shockwave on the deflector and reduces the duration and range of the pressure

 doi:10.20944/preprints202404.1760.v1

disturbances on the deflector surface. Therefore, the integrated dual-sided deflector system demonstrates superior improvement in terms of inhibiting the range and intensity of pressure disturbances compared to the conventional cooling system.

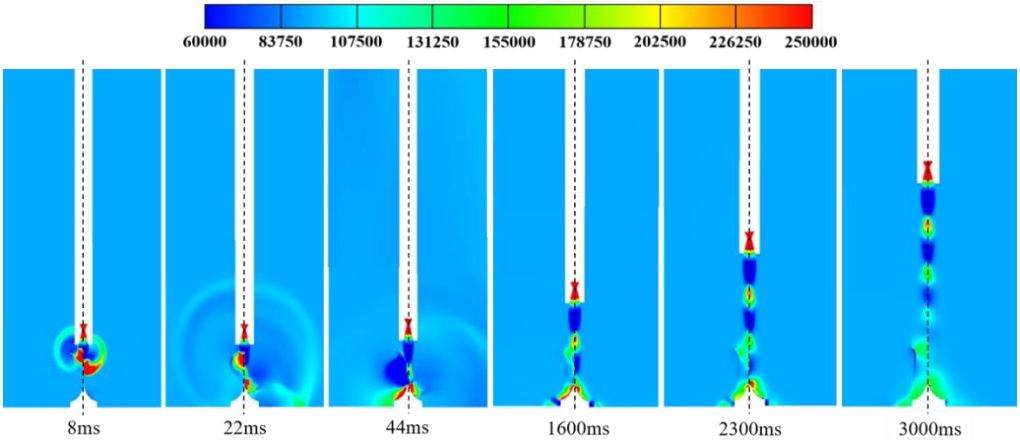

Figure 13. Comparison of pressure distribution under the integrated dual-sided deflector system and the conventional cooling system (unit: Pa) (the left side is the conventional cooling system, and the right side is the integrated dual-sided deflector system).

(2) Temperature Variation Process

The variation of temperature in the near-ground flow field at the launch site is highly dependent on the parameters and flow characteristics of the gas jet. When the gas jet is injected at high velocity from the rocket engine nozzle, it carries high-temperature combustion products and thermal energy [37]. When interacting with the surrounding air and solid surfaces, it triggers complex flow phenomena, resulting in the propagation and alteration of temperature within the flow field.

Figure 14 illustrates the temperature distribution in the *oxy*-symmetric plane of the flow field affected by the integrated dual-sided deflector system. From the figure, it can be observed that throughout the entire development of the gas jet's main flow, there is no significant accumulation of high heat flux density observed on the deflector surface and its surrounding ground area. Instead, these regions remain at relatively low temperatures. The main reason for this phenomenon is the convective interaction between the downward vertical gas jet and the upward vertical liquid water jet. On one hand, the water jet is "captured" and vertically compressed by the gas jet, leading to intense momentum exchange and the dissipation of a significant amount of energy, including that of the high-temperature gas. On the other hand, the liquid water jet injected from the deflector's surface continuously undergoes compression and changes in flow direction. This gradually forms a layer of liquid water "film" on the deflector's surface and its surrounding ground area (Figure 10), effectively isolating the high-temperature gas jet from direct contact with the deflector surface and weakening its impact on the deflector. It can be concluded that the integrated dual-sided deflector system not only significantly reduces the thermal load impact intensity of the gas jet on the deflector, but also effectively performs insulation and cooling, improving the temperature environment in the near-ground flow field.

 doi:10.20944/preprints202404.1760.v1

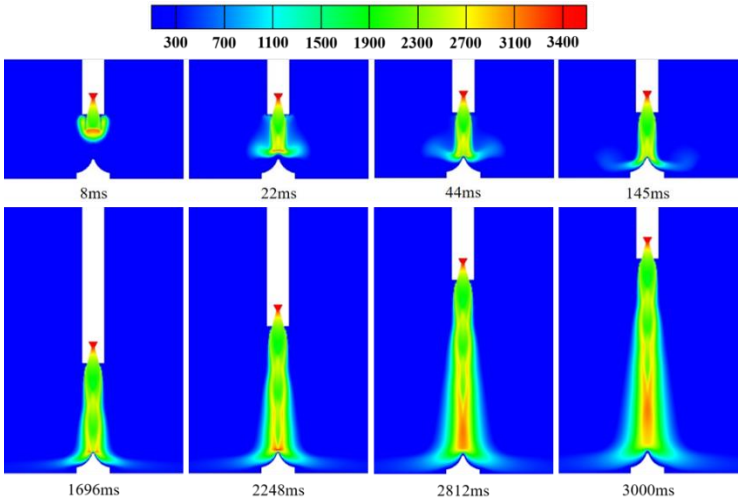

Figure 14. Temperature distribution in the *oxy* symmetry plane under the integrated dual-sided deflector sysytem (unit: K).

Figure 15 presents a comparison of temperature distribution in the flow field between the conventional cooling system and the integrated dual-sided deflector system. From the figure, it can be observed that the conventional cooling system restricts the diffusion of high-temperature gas into the surrounding space, significantly reducing the range of areas near the ground affected by high-temperature gas. Specifically, there are no high-temperature regions near the ground in the vicinity of the dual-sided deflector. However, the surface of the deflector, especially the top and mid-body regions, still experiences prolonged and intense thermal load impact effects. In contrast, the integrated dual-sided deflector system effectively suppresses the dynamic thermal load impact of the high-temperature gas on the deflector. The convective interaction between the liquid water jet and the gas jet forms a protective "water film" on the surface of the deflector and its surrounding ground area (Figure 10). This directly blocks the impact of high-temperature gas, preventing the deflector surface from being enveloped by high-temperature gas and maintaining it at a lower temperature state throughout. Therefore, the integrated dual-sided deflector system demonstrates superior improvement in terms of enhancing the temperature environment in the near-ground flow field and providing active thermal protection for the deflector.

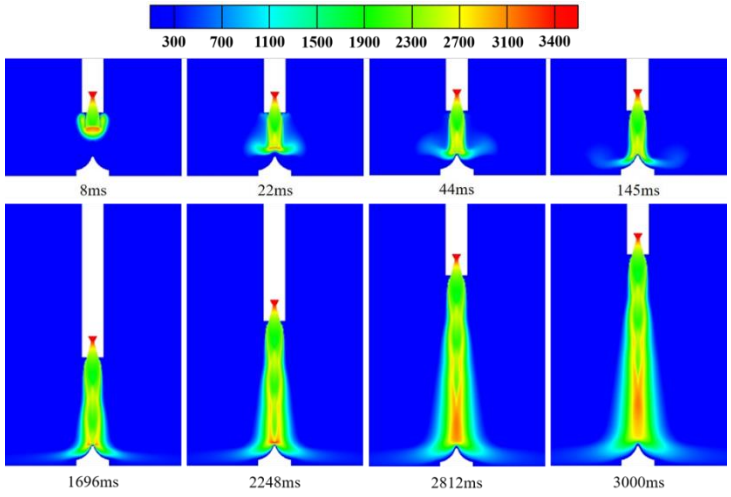

Figure 15. Comparison of temperature distribution under the integrated dual-sided deflector system and the conventional cooling system (unit: K) (the left side is the conventional cooling system, and the right side is the integrated dual-sided deflector).

 doi:10.20944/preprints202404.1760.v1

To provide a more intuitive illustration of the superior thermal protection effect of the integrated dual-sided deflector system for the deflector, Figure 16 presents a comparison of temperature distribution maps on the deflector surface for three different scenarios. In each set of three maps corresponding to a specific moment, the leftmost map represents the traditional dual-sided deflector (traditional), the middle map represents the conventional cooling system (conventional), and the rightmost map represents the integrated dual-sided deflector system (integrated). Under the traditional dual-sided deflector, the deflector is subjected to severe thermal load impact from the gas jet during the initial stage of rocket launch. When the gas jet impacts the top of the deflector, it stagnates and forms a relatively high-temperature "core" region due to the obstruction of the top structure. Subsequently, this high-temperature "core" region spreads towards the surfaces of the deflector on both sides in an elliptical shape. At 1600 ms, high-temperature regions (2500K to 3400K) with a "hexagonal" distribution form on the surfaces of the deflector, and the temperature at the top of the deflector reaches 3400K, while the temperature in the mid-body and downstream regions is around 3000K. At 2300 ms, the high-temperature region on the deflector surface expands further, changing from a "hexagonal" shape to a "trapezoidal" shape. The temperature at the top, mid-body, downstream, and step regions of the deflector all reach 3400K. The thermal environment of the dual-sided deflector is extremely harsh. As the altitude of the launch vehicle increases, the surface temperature of the deflector gradually decreases and exhibits a more uniform distribution. However, the overall deflector still remains at high temperatures, with the highest temperature reaching close to 2100K.

Compared to the traditional dual-sided deflector, the conventional cooling system in Figure 16 exhibits a delay of approximately 40ms in the appearance of high-temperature gas on the deflector surface. Furthermore, there is a noticeable change in the distribution of high-temperature regions on the deflector surface, transitioning from the original "hexagonal" and "trapezoidal" shapes to "quadrilateral" and "U-shaped" patterns. Additionally, due to the lateral impact and vaporization reaction of liquid water, a significant amount of energy is consumed from the high-temperature gas, reducing the impact of dynamic thermal load from the gas jet on the side edges, downstream, and step regions of the deflector. This, to some extent, improves the thermal environment on the deflector surface. However, due to the continuous impact of the gas jet core region, the regions at the top middle and mid-body of the deflector remain at high temperatures (3000K to 3400K) for a prolonged period.

In comparison to the traditional dual-sided deflector and the conventional cooling system, the integrated dual-sided deflector system effectively mitigates the intense thermal load impact from the gas jet, providing superior thermal protection for the deflector. Throughout the complete development process of the gas jet mainstream, the integrated dual-sided deflector system disperses and guides the high-temperature gas jet through the convective impact of the gas-liquid two-phase flow, reducing the concentration of high heat flux on the deflector surface. Additionally, the "water film" formed by liquid water acts as insulation for cooling, resulting in a uniform temperature distribution on the deflector surface, consistently maintaining it at a lower temperature state. This effectively prevents excessive heating of the dual-sided deflector.

Preprints.org (www.preprints.org) | NOT PEER-REVIEWED | Posted: 26 April 2024 doi:10.20944/preprints202404.1760.v1

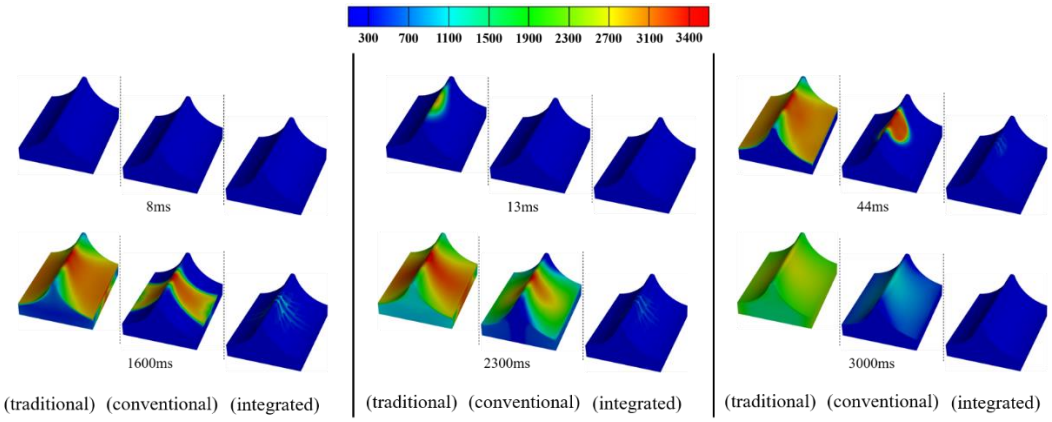

Figure 16. Comparison of deflector surface temperature distribution under three different scenarios (unit: K).

To quantitatively analyze the optimal improvement effect of the integrated dual-sided deflector system on the convective temperature environment, Figure 17 presents the variation curves of the maximum temperatures on the bottom surface of the rocket body and the surface of the deflector over time for three different scenarios. From Figure 17(a), it can be observed that the integrated dual-sided deflector system significantly reduces the fluctuation range of the maximum temperature curve on the bottom surface of the rocket body, delays the occurrence of the peak, and the peak value is much lower than the other two scenarios. The reason for the higher peak value in the conventional cooling system compared to the traditional dual-sided deflector is that the former has the liquid water injection nozzle located near the engine exhaust. The impact and squeezing effect of the liquid water column on the gas jet exacerbate the "rolling" phenomenon of the gas, resulting in an increase in temperature on the bottom surface of the rocket body. In the mid-stage of flow development, after the temperature curve on the bottom surface of the rocket body monotonically decreases to its minimum value, it shows a slight oscillation and upward trend. At this point, the minimum temperature value of the conventional cooling system is significantly lower than the other two scenarios, but the temperature differences among the three scenarios are not large and all remain below 580K. In the late stage of flow development, the variation curves of the maximum temperature on the bottom surface of the rocket body for all scenarios overlap and stabilize at around 530K.

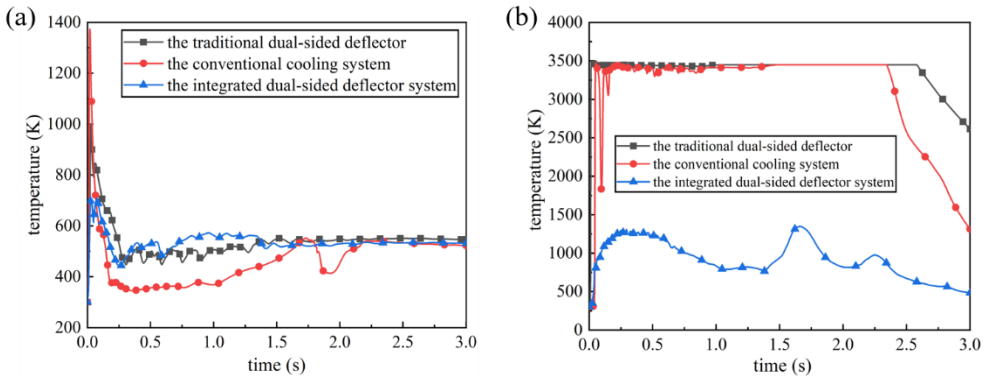

Figure 17. Comparison of maximum temperature variation curves at the launch vehicle bottom and deflector surface: (a) the bottom of rocket; (b) the surface of deflector.

To quantitatively demonstrate the superior thermal protection provided by the integrated dual-sided deflector system for convective cooling and thermal protection of the deflector, the data of temperature variation over time for seven monitoring points P11 to P41 and P22 to P44 on the deflector surface in Figure 6 are extracted, and the temperature curves of these points for the three different scenarios are compared as shown in Figure 18. It should be noted that monitoring point P11,

 doi:10.20944/preprints202404.1760.v1

located at the liquid water injection nozzle position on the deflector surface, maintains a constant temperature value of 300K and is not plotted in Figure 18(c). Throughout the entire development process of the gas flow field, a comparison of Figure 18(a), (b) and (c) reveals that under the traditional dual-sided deflector, except for monitoring point P41, the temperature curves of the other monitoring points on the deflector surface remain within the range of approximately 2000K to 3400K. Under the conventional cooling system, the temperature on the deflector surface near the side edges exhibits slight oscillation and remains around 500K. The temperature curve of the deflector surface at the mid-body position fluctuates around 2000K, while the temperature near the *oxy*-axisymmetric plane remains at a high temperature state of 2500K to 3400K for a prolonged period. In comparison to the other two scenarios, the temperature variation curves on the deflector surface for the integrated dual-sided deflector system show significant reduction, with none of the curves exceeding 750K. In particular, the temperature curves for monitoring points P21, P31, and P41 consistently remain below 450K. This indicates that the integrated dual-sided deflector system can more effectively optimize and regulate the temperature environment on the deflector surface. Compared to the other two scenarios, it demonstrates superior thermal protection for the deflector surface.

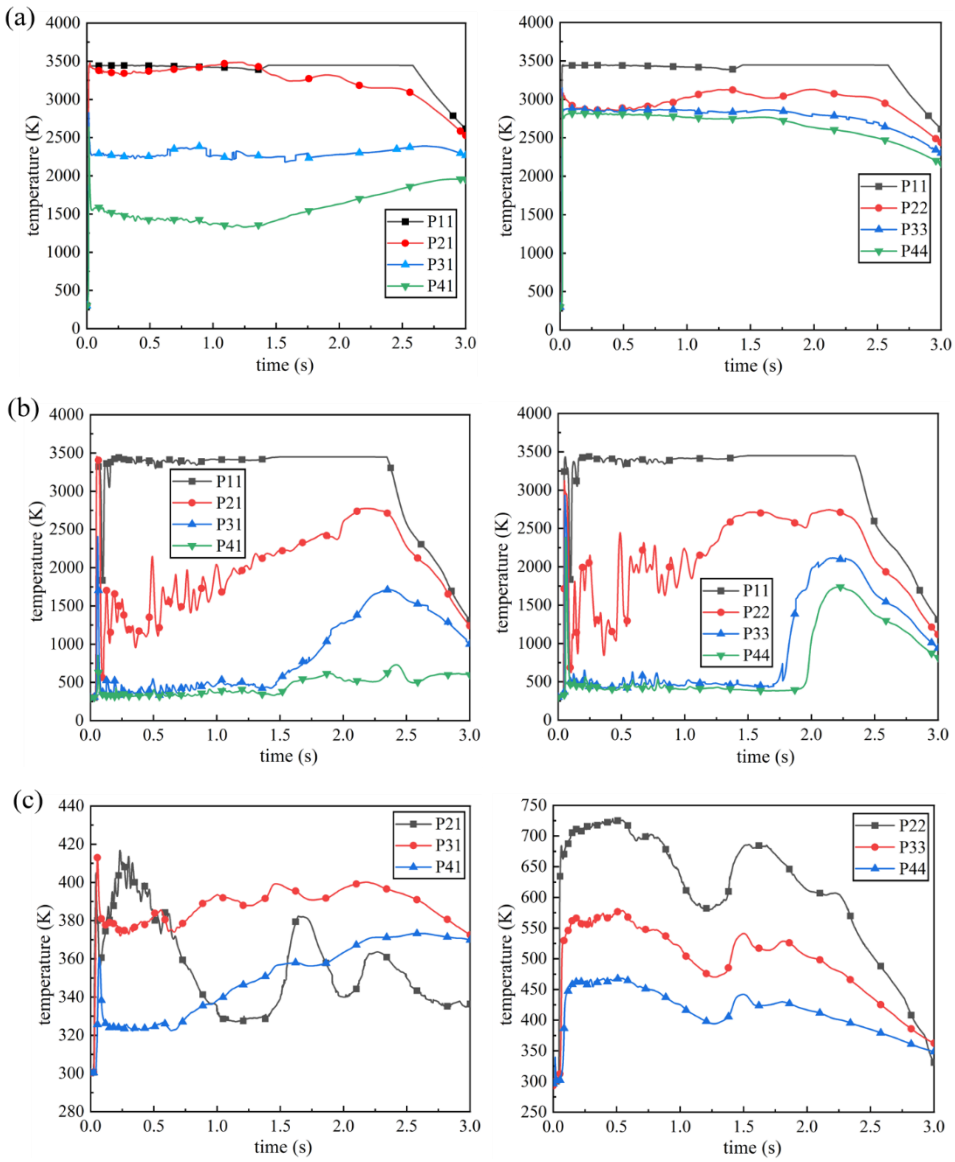

Figure 18. Comparison of temperature variation curves at various monitoring points on the deflector surface: (a) the traditional dual-side deflector; (b) the conventional cooling system; (c) the integrated dual-side deflector.

 doi:10.20944/preprints202404.1760.v1

The peak temperature values of the temperature curves on the deflector surface for the three different scenarios in Figure 18 are summarized and presented in Table 3. The temperature reduction percentage of the peak values is calculated relative to the traditional dual-sided deflector (traditional), serving as the baseline. From Table 3, it can be observed that the integrated dual-sided deflector system (integrated) exhibits a significantly greater reduction in the peak temperature values on the deflector surface compared to the conventional cooling system (conventional). The temperature reduction percentages for the former range from 76.86% to 91.29%, while the maximum reduction percentage for the latter is only 23.14%. Therefore, it can be concluded that the integrated dual-sided deflector system demonstrates superior performance in improving the temperature environment on the deflector surface.

Table 3. Comparison of maximum temperature values at various monitoring points on the deflector surface.

the monitoring points	traditional temperature (K)	conventional temperature (K)	integrated temperature (K)	conventional percentage reduction	integrated percentage reduction
P11	3446.08	3419.80	300	0.76%	91.29%
P21	3485.52	3445.16	416.73	1.16%	88.05%
P31	2820.63	2376.82	413.11	15.73%	85.35%
P41	2642.29	836.62	359.83	13.62%	86.39%
P22	3133.88	3132.35	725.08	23.14%	76.86%
P33	3152.55	2897.58	578.36	18.35%	81.65%
P44	3035.03	2360.15	468.71	15.44%	84.56%

In summary, the integrated dual-sided deflector system has a significant impact on the temperature variation process in the near-ground space of the launch site and effectively improves the temperature environment on the deflector surface. Through qualitative and quantitative comparative analysis of the thermal protection effectiveness of the deflector and its surface temperature variation curves, the superior performance of the integrated dual-sided deflector system in reducing the flow field temperature, suppressing temperature fluctuations, and providing long-lasting thermal protection has been validated. These improvements are crucial for ensuring the stability of the flow field, protecting ground launch equipment and facilities from the influence of high-temperature gases, and enhancing the operational efficiency of the ground launch system in space launch facilities.

(3) The degree of vaporization of liquid water

In the region exposed to high-temperature gas jet, liquid water undergoes intense vaporization, generating a large amount of water vapor. On one hand, the liquid water undergoes an endothermic phase change, consuming a significant amount of energy, including the initial shockwave and high-temperature gas. On the other hand, the generated water vapor partially dilutes the high-temperature gas, alleviating the accumulation of high heat flux density near the surface of the deflector and the surrounding ground area. During vehicle launching, the degree of vaporization of liquid water varies significantly depending on the chosen thermal protection and cooling scheme.

Figure 19 illustrates the distribution of liquid water vaporization phenomena within the temperature field affected by the conventional cooling system. The black contour lines in the figure represent the locations and extent of vaporization reactions of liquid water. After the high-temperature gas jet is rapidly impacted onto the liquid water column upon engine exhaust, significant vaporization reactions occur at the gas-liquid interface, with a maximum vaporization reaction rate of 0.1703 kg/(m^3·s). When the gas jets impinge on the deflector, fully covering the top surface, residual liquid water on the deflector surface undergoes vaporization reactions, with a

 doi:10.20944/preprints202404.1760.v1

maximum vaporization reaction rate of 0.4550 kg/(m³·s). Subsequently, as the gas jet diffuses and flows towards the ground, the vaporization zone of liquid water exhibits an "X-shaped" distribution pattern. As the rocket continues to accelerate upward, the vaporization reaction region gradually takes on an "eight-shaped" distribution, expanding along the trajectory of the gas jet. At this stage, the maximum vaporization reaction rate of the liquid water is 1.8029 kg/(m³·s).

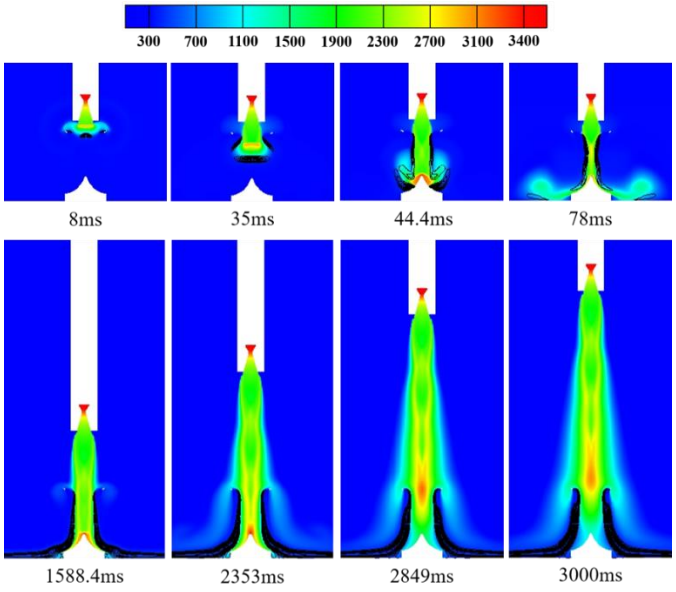

Figure 19. Temperature distribution in gas-liquid two-phase flow field under the conventional cooling system (unit: K) (the black contour in the figure is the rate of vaporization reaction of liquid water, unit: kg/(m³·s)).

Unlike the conventional cooling system, the integrated dual-sided deflector system has its water spray system located on the deflector. This results in a significant change in the location of the vaporization reaction zone of liquid water within the flow field. Figure 20 illustrates the distribution of liquid water vaporization phenomena within the temperature field affected by the integrated dual-sided deflector system. At the initial ignition of the engine, the high-temperature gas and liquid water move towards each other without making contact, resulting in minimal vaporization phenomena within the flow field. When the convective impact occurs between the liquid water jet and the gas jet, vaporization reactions take place at the gas-liquid interface, with a maximum vaporization reaction rate of 5.8552 kg/(m³·s). Subsequently, as the gas jet diffuses and flows onto the surface of the deflector, the liquid water gradually covers the deflector surface. The vaporization reaction zone exhibits two different distribution patterns, namely a "W-shaped" and an "eight-shaped" distribution along the deflector's surface. The maximum vaporization reaction rate reaches 13.3604 kg/(m³·s). When the gas flow further diffuses to the ground area away from the deflector, the liquid water has spread across the deflector surface and the surrounding ground region. The distribution range of the vaporization reaction zone expands, with a maximum vaporization reaction rate of 13.7594 kg/(m³·s). As the rocket accelerates upward to higher positions, the gas jet core gradually moves away from the deflector, resulting in a reduction in the vaporization reaction zone of the liquid water. At this stage, the maximum vaporization reaction rate is 11.9659 kg/(m³·s).

 doi:10.20944/preprints202404.1760.v1

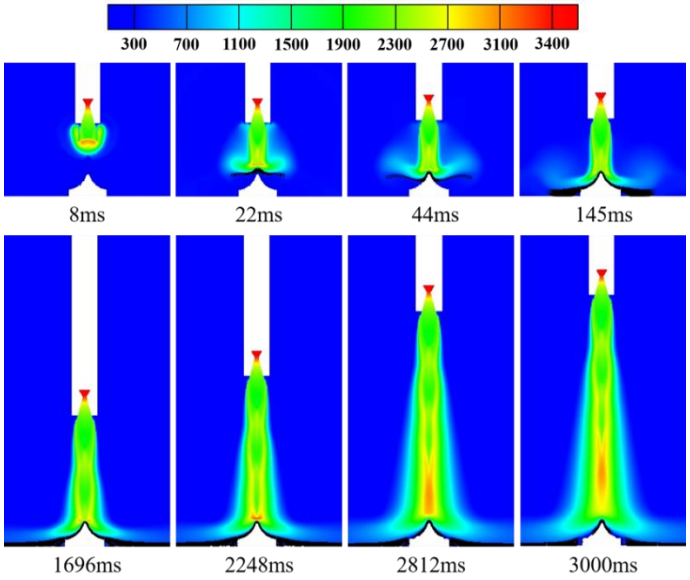

Figure 20. Temperature distribution in gas-liquid two-phase flow field under the integrated dual-sided deflector system (unit: K) (the black contour in the figure is the rate of vaporization reaction of liquid water, unit: kg/(m^3·s)).

A comprehensive comparison between Figure 19 and Figure 20 reveals that the maximum vaporization reaction rate of liquid water within the flow field affected by the integrated dual-sided deflector system is significantly higher than that of the conventional cooling system. In the former case, the maximum value reaches 13.7594 kg/(m^3·s), while in the latter case, it is only 1.8029 kg/(m^3·s). This indicates that compared to the conventional cooling system, the integrated dual-sided deflector system, with the continuous injection of liquid water jet through the surface orifices of the deflector, significantly increases the contact area between the gas and liquid phases. This, in turn, enhances the degree of vaporization of liquid water within the flow field, effectively reducing the temperature and heat flux density of the flow field, and achieving optimal improvement in the flow field environment.

V. Results and Discussion

To address the issue of intense erosion and ablation of the deflector by the gas jet during the hot launch of a launch vehicle, an integrated dual-sided deflector system for convective cooling and thermal protection of the flow field is proposed. This system involves the installation of a water spray system on the deflector to improve the flow field environment by implementing a bottom-up water spray method on the gas jet. The interaction mechanism between liquid water and the gas jet, as well as the effectiveness of flow field improvement, are thoroughly investigated using the CFD method. Through a comparative analysis with the traditional dual-sided deflector and the conventional cooling system, the feasibility of the integrated dual-sided deflector system in providing active thermal protection for the deflector is validated. The main conclusions obtained are as follows.

(1) Regarding the heat transfer during the phase change of compressible gas-liquid two-phase flow, and the varying distribution of different bubble shapes and sizes at the gas-liquid interface, a modified Lee model is derived that incorporates bubble parameter factors. The rationality and accuracy of the phase change mass transfer coefficient can be achieved by adjusting the equivalent diameter and shape factor of the bubbles. The effectiveness of the improved vaporization model is validated through multiphase flow experiments involving gas jet injection and water. The results demonstrate that the modified Lee model exhibits higher agreement with experimental data compared to the classical Lee model. In other words, the modified Lee model

 doi:10.20944/preprints202404.1760.v1

significantly enhances the accuracy of numerical calculations for heat and mass transfer in gas-liquid two-phase flow processes.

(2) In the gas flow field affected by the integrated dual-sided deflection device, there is a very distinct boundary between the gas and liquid phases, with the liquid water continuously adhering beneath the mainstream of the gas jet. Considering the hindrance of pressure disturbance propagation, regulation of temperature changes, and improvement of the thermal environment of the deflector, the integrated dual-sided deflector system provides a more stable, controllable, and reliable flow field environment during the hot launch of a rocket. The primary mechanisms for thermal protection and cooling can be summarized as follows:

Through the convective impact between the gas jet and the liquid water jet, there is a strong momentum exchange between the gas and liquid phases, which consumes a significant amount of energy in the flow field, including the initial shock wave, and significantly reduces the propagation range and intensity of pressure disturbances. By absorbing energy from the flow field through the vaporization of liquid water, the dilution of high-temperature gas by water vapor, and the impact and compression of the gas jet by the liquid water jet, the thermodynamic impact of the gas jet on the deflector is suppressed, effectively improving the temperature environment of the near-ground flow field. Through the continuous impact and compression of the gas jet, the liquid water covers the surface of the deflector and the nearby ground area, and forms a layer of "water film". This not only greatly reduces the dynamic load impact intensity of the gas jet on the dual-sided deflector, but also effectively prevents direct contact between the high-temperature gas and the deflector surface, increasing the contact area between the gas and liquid phases and improving the utilization of liquid water in the flow field.

It can be stated that the integrated dual-sided deflector system for cooling and thermal protection of the flow field exhibits significant performance advantages in the regulation of gas diffusion flow and improvement of the flow field environment in the near-ground area of the launch site. Particularly, in terms of the thermal environment of the dual-sided deflector, it achieves effective gas exhaust and deflection while reducing the impact load of the gas jet on the deflector, thereby achieving the desired design objectives and realizing the active thermal protection of the dual-sided deflector. However, further research is needed to obtain optimal design parameters for the new water spray system by studying the influence of various water spray factors on the effectiveness of flow field improvement.

References

1. Kristian, R.; Christophe, D. Heat transfer and associated coherent structures of a single impinging jet from a round nozzle," International Journal of Heat and Mass Transfer, 2021,173, 121197.
2. Dalle, D. J.; Rogers, S. E.; Meeroff, J. G.; Burkhead, A. C.; D. G. Schauerhamer; Diaz, J. F. Launch vehicle ascent computational fluid dynamics for the space launch system. Journal of Spacecraft and Rockets, 2023: 1-14.
3. Faheem, M.; Khan, A.; Kuma, R.; Khan, S. A.; Asrar, W.; Sapardi, A. M. Experimental study on the mean flow characteristic of a supersonic multiple jet configuration. Aerospace Science and Technology, 2021, 108, 106377.
4. Norris, R. S.; Kristensen, H. M. Nuclear U.S and Soviet/Russian intercontinental ballistic missiles. Bulletin of the Atomic Scientists, 2009, 65(1), 62-69.
5. Vu, B. T.; Bachchan, N.; Peroomian, O.; Akdag, V. Multiphase modeling of water injection on flame deflector. Proceedings of the 21st AIAA Computational Fluid Dynamics Conference, San Deigo, US, 2013.
6. Li, J.; Jiang, Y.; Yu, S. Z.; Zhou, F. Cooling effect of water injection on a high-temperature supersonic jet. Energies, 2015, 8(11), 13194-13210.

 doi:10.20944/preprints202404.1760.v1

7. Lu, C. Y.; Zhou, Z. T.; Shi, Y.; Bao, Y. Y.; Le, G. G. Numerical simulations of water spray on launch pad during rocket launching. Spacecraft and Rockets, 2021, 58, 566-574.
8. Zhou, Z. T.; Lu, C. Y.; Zhao, C. F.; Le, G. G. Numerical simulations of water spray on flame deflector during the four-engine rocket launching. Advances in Space Research, 2020, 65, 1296-1305.
9. Zhou, Z. T.; Zhang, L. J.; Le, G. G. Numerical study for the flame deflector design of four-engine liquid rockets. Engineering Applications of Computational Fluid Mechanics, 14(1), 2020, 726-737.
10. Zhou, Z. T.; Sun, P. J.; Bao, Y. Y. Numerical simulations of thermal environment of the rocket impingement jet with afterburning under different water spray angles. Aerospace Science and Technology, 2022, 121, 107308.
11. Ji, T. Y. Numerical Study on Water Injection Cooling of Gas Plume in Solid Rocket Motor. Harbin Engineering University, 2020.
12. Xiong, Y. Numerical Simulation Study on High Temperature Gas Cooling System of Solid Rocket Motor. Academy of Aerospace Solid Propulsion Technology, 2021.
13. Luo, T. P.; Liu, R. M.; Li, M.; Zhang, J. X. Numerical study on spray cooling of test bench flow channel based on DPM. Aerospace Power, 2018, 33(2), 497-507.
14. Fang, B.; Zhao, T. S. The “Starship” explosion aftermath appearance of the launch pad damage. Beijing Business News, 2023:8.
15. Zhang, W.; Liu, J. J.; Liu, W.; Jin, X. Smart dragon 3 launch vehicle system. Aerospace China, 2022, 23(4), 3-10.
16. Zhang, M. M.; Jiang, Y.; Shi, S. Y.; Deng, Y. G. Influence on flow field of hot launch in a W-shaped underground space by water injection. Journal of Acta Armamentarii, 2023, 44(4), 1158-1170.
17. Lee, W. H. A pressure iteration scheme for two-phase flow modeling. Computational Methods for Two-Phase Flow and Particle Transport, Toh Tuck Link, Singapore: World Scientific, 1979: 61-82.
18. Hertz, H. On the evaporation of liquids, especially mercury, in vacuo. Annalen der Physik, 1882,17: 177.
19. Knudsen, M. Maximum rate of vaporization of mercury. Annalen der Physik, 1915, 47: 697.
20. Da, R. E.; Del, C. D. Numerical simulation of laminar liquid film condensation in a horizontal circular minichannel. Journal of Heat Transfer-Transactions of the ASME, 2012, 135(5), 1-8.
21. Da, R. E.; Del, C. D.; Garimell, S. V.; Cavallini, A. The importance of turbulence during condensation in a horizontal circular minichannel. International Journal of Heat Transfer, 2012, 55(13/14): 3470-3481.
22. Deschepper, C. K.; Heynderickx, G. J.; Marin, G. B. Modeling the evaporation of a hydrocarbon feedstock in the convection of a steam cracker. Computers and Chemical Engineering, 2009, 33:122-132.
23. Wu, H. L.; Peng, X. F.; Ye, P.; Gong, Y. E. Simulation of refrigerant flow boiling in the serpentine tubes. International Journal of Heat and Mass Transfer, 2007, 50: 1186-1195.
24. Bortolin, S.; Da, R. E.; Del, C. D. Condensation in a square minichannel: application of the VOF method. Heat Transfer Engineering, 2014, 35(2), 193-203.
25. Qiu, G. D.; Cao, W. H.; Wu, Z. Y.; Jiang, Y. Analysis on the value of coefficient of mass transfer with phase change in Lee’s equation. Journal of Harbin institute of technology, 2014, 46(12), 15-19.
26. Chen, G.; Nien, T. T.; Yan, X. H. An explicit expression of the empirical factor in a widely used phase change model. International Journal of Heat and Mass Transfer, 2020,150, 119279.
27. Wang, X. D. Model study of mass transfer at gas-liquid interface. Hunan: Xiangtan University, 2021.
28. Fu, J. Analytical Model Development and Numerical Simulation of Gas-Liquid Interface Mass Transfer. Hunan: Xiangtan University, 2017.

 doi:10.20944/preprints202404.1760.v1

29. Zhou, Y. Q.; Wang, W. W.; Duan, J. H. Research progress on bubble motion behavior in liquids. Petroleum Refinery Engineering, 2023, 53(09), 5-8.
30. Shen, Y.; Zhang, L. L.; Wu, Y. R.; Chen, W. Z. The role of the bubbles- bubble interaction on radial pulsations of bubbles. Ultrasonics Sonochemistry, 2021, 73: 105535.
31. Li, W. P.; Cao, S. Y.; Liu, X. N. Effects of grain shape on incipient motion of non-uniform sediment. Advances in Water Science, 2007, 3: 342-345.
32. Xiao, Y.; Meng,;M.; Daouadji, A.; Chen, Q. S.; Wu, Z. J.; Jiang, X. Effects of particle size on crushing and deformation behaviors of rockfill materials. Geoscience Frontiers, 2020, 11(2), 375-388.
33. Lv, Y. R.; Wang, C.; Huang, H. X.; Zuo, D. J. Study on particle structure and crushing behaviors of coral sand. Rock and Soil Mechanics, 2021, 42(02), 352-360.
34. Zhan, G. Design and research of gas-liquid booster pump. Shanghai: Donghua University, 2024.
35. Zhou, P. Design on hydraulic pressure boosting system for forging press. Forging & Stamping Technology, 2024, 49(1), 189-195.
36. Wang, W. P.; Liu, F. S.; Zhang, N. C. Structural transformation of liquid water under shock compression condition. Acta Phys. Sin, 2014, 63(12), 270-274.
37. Zhang, X. W.; Pan, L.; Wang, L.; Zou, J. J. Review on synthesis and properties of high-energy-density liquid fuels: hydrocarbons, nanofluids and energetic ionic liquids. Chemical Engineering Science, 2018, 180, 95-125.